coatings

MDPI

Article

A Study on the Mechanism by Which Graphene Oxide Affects the Macroscopic Properties and Microstructure of Abrasion-Resistant Ultra-High-Performance Concrete (UHPC)

Tusheng He [1,2], Wei Xie [3,4], Feng Wang [5], Zi Yu [3], Fang Xu [6], Jinhui Li [3,4,*], Yitong Deng [1,7], Qingjun Ding [1,7,*], Yan Hao [3,4], Wei Xu [6] and Haibin Yu [6]

1 State Key Laboratory of Silicate Materials for Architectures, Wuhan University of Technology, Wuhan 430070, China; hts0539@163.com (T.H.); yitongdeng2022@163.com (Y.D.)
2 School of Chemistry and Civil Engineering, Shaoguan University, Shaoguan 512005, China
3 College of Materials Science and Engineering, Wuhan Textile University, Wuhan 430200, China; 18486501844@163.com (W.X.); yu1018541283@163.com (Z.Y.); m18772447232@163.com (Y.H.)
4 State Key Laboratory of New Textile Materials and Advanced Processing Technologies, Wuhan 430200, China
5 Guangdong Gezhouba Zhao Ming Expressway Co., Ltd., Zhaoqing 526123, China; wf601@163.com
6 Faculty of Engineering, China University of Geosciences, Wuhan 430074, China; xufang@cug.edu.cn (F.X.); 13871526941@139.com (W.X.); yu15826723351@163.com (H.Y.)
7 School of Materials and Science Engineering, Wuhan University of Technology, Wuhan 430070, China
* Correspondence: lijinhui-2001@163.com (J.L.); dingqj2003@whut.edu.cn (Q.D.)

Abstract: To further enhance the abrasion resistance of UHPC in demanding abrasion environments, this study investigated the effects of graphene oxide (GO) on the workability, mechanical properties, and abrasion resistance of UHPC. Utilizing 27Al Nuclear Magnetic Resonance (NMR), 29Si NMR, microhardness, and BET analysis, the study analyzed the mechanisms through which GO influences UHPC's microstructure in terms of abrasion resistance. Additionally, molecular dynamics simulations were employed to examine the mechanisms by which GO enhances UHPC's abrasion resistance at the nano and micron scale. The findings show that an optimal amount of GO can improve the mechanical properties and abrasion resistance of UHPC. When 0.03% of GO (by cementitious material mass) was incorporated, the impact on workability was minimal, yet compressive strength increased by approximately 1.80%, flexural strength by 3.02%, impact wear resistance by 1.78%, the abrasion loss rate decreased by 10.01%, ultimate impact energy increased by 1.76%, and the toughness index improved by 10.10%. GO enhances abrasion-resistant UHPC primarily by increasing hydration, refining pore structure, and improving the microstructure of the interfacial transition zone. While GO increases the hydration degree of the UHPC matrix, it does not alter the silicate chain in C-A-S-H gels within the paste. Additionally, the incorporation of graphene oxide can refine the pore structure of the UHPC cement paste and improve the microstructure of the interfacial transition zone (ITZ) between the aggregate and the cement paste. The molecular dynamics simulation reveals that, under abrasive forces, GO forms strong, stable chemical bonds with the C-A-S-H base atoms, significantly enhancing the abrasion resistance of C-A-S-H.

Keywords: graphene oxide; UHPC; abrasion resistance; microstructure; molecular dynamics simulations

Citation: He, T.; Xie, W.; Wang, F.; Yu, Z.; Xu, F.; Li, J.; Deng, Y.; Ding, Q.; Hao, Y.; Xu, W.; et al. A Study on the Mechanism by Which Graphene Oxide Affects the Macroscopic Properties and Microstructure of Abrasion-Resistant Ultra-High-Performance Concrete (UHPC). *Coatings* **2024**, *14*, 1482. https://doi.org/10.3390/coatings14121482

Academic Editor: Gianfranco Carotenuto

Received: 16 October 2024
Revised: 11 November 2024
Accepted: 20 November 2024
Published: 23 November 2024

1. Introduction

In the mountainous regions of western China, debris flows and floods can lead to the rapid erosion, abrasion, and brittle damage of concrete structures, causing significant aging of these structures after only 1–2 years of service [1–4]. Ultra-high-performance concrete (UHPC) is an advanced cement-based material known for its exceptional strength,

remarkable durability, high toughness, and superior abrasion resistance [5–16]. It offers a novel selection of materials for the design and reinforcement of bridges in the rugged mountainous regions of the western areas. The fundamental principle lies in the concept of densely packed particles, utilizing a fine aggregate like quartz sand, along with admixtures such as silica fume, to enhance the bulk density of cement-based materials, thereby achieving a compact structure. Furthermore, matrix toughness is enhanced by fiber incorporation. Consequently, this material exhibits remarkable mechanical properties and impermeability.

In order to address the durability issues of bridge piers caused by abrasion in the western mountainous areas, an abrasion-resistant UHPC has been developed by optimizing the material's composition and controlling its microstructure. Based on extensive experimental research, this experiment utilized fully saturated high-strength abrasion-resistant porous pre-wetted high-titanium heavy slag sand and modified rubber particles as raw materials [17,18]. The modified rubber particles can enhance the toughness, crack resistance, durability, impact resistance, and fatigue resistance of UHPCs by altering their surface morphology, increasing hydrophilicity, and strengthening the interfacial bond with the cement matrix. The internal curing and arch effect of pre-wetted high-titanium heavy slag sand, along with the combined effect with the expansion agent, further enhanced the abrasion resistance and volume stability of UHPC. Additionally, the synergistic toughening effect of fibers and modified rubber particles further enhanced the impact resistance of UHPC.

However, in the western mountainous areas, certain specific components must endure extremely high impact forces, which requires the further development of abrasion-resistant ultra-high-performance concrete with superior impact resistance and toughness. Previous research has demonstrated that nanomaterials like graphene oxide (GO) [19–27] and carbon nanotubes (CNT) [28,29] can enhance the impact resistance and microstructure of cement-based materials. Although GO and CNTs exhibit excellent properties, they tend to aggregate and clump when incorporated into cement-based matrices as a reinforcement material, making it challenging to achieve uniform dispersion throughout the paste. Lu Shenghua, Zhang Di et al. [30–34] studied the microstructures and mechanisms of GO-reinforced and toughened cement-based composites. The findings indicate that GO can shape and densify hydration products in cement, promoting regular crystal formation and significantly improving the macroscopic performance of such composites. To address/solve the problem of the uniform dispersion of GO within cement-based materials, Lv Shenghua and Yang Lingjun et al. [35,36] explored methods including admixture addition and ultrasonic dispersion to improve its homogeneity in cement-based materials.

Recently, scholars have conducted studies on the application of GO in UHPC. W. Meng et al. [37,38] investigated the fluidity, hydration characteristics, shrinkage, mechanical properties, and microstructure of UHPC incorporating graphene nanosheets. The results indicate that different sizes of graphene nanosheets have varying effects on the mechanical properties of UHPC. However, a similar trend is observed. Graphene nanosheets effectively enhance the axial tensile strength, flexural strength, energy absorption capacity, and single-wire pull-off strength of UHPC. The addition of graphene nanosheets leads to reduced fluidity and porosity in UHPC. Ren Zhaofeng et al. [39] examined the influence of GO on the performance of ultra-high-performance cement-based materials using a mix design similar to conventional UHPC. The research findings demonstrate that GO improves mechanical properties but decreases fluidity in ultra-high-performance cement-based materials. Lanzhen Yu et al. [25] explored the impact of GO on recycled fine aggregate-based UHPC and found that its addition enhances both mechanical properties and durability while increasing self-shrinkage.

In conclusion, GO is currently undergoing laboratory experimental research on cement mortar and ordinary concrete, with a focus on investigating the impact of GO on the performance of concrete and its underlying mechanisms. However, there is limited

research regarding the effects of GO on the performance of UHPC, as well as the influence of GO on the abrasion resistance of UHPC and the impact on its microstructure.

Previous studies have demonstrated that the anti-cracking effect of hybrid fibers and the deformation and energy absorption of modified rubber particles can significantly enhance the toughness and impact resistance of UHPC at a macroscopic scale. GO was doped into UHPC to achieve the multi-scale toughening of UHPC and improve the toughness of the paste at the nanoscale and micron scale, as well as to enhance the interface structure. This research investigates the influence of GO on the mechanical properties, impact resistance, and abrasion resistance of abrasion-resistant UHPC. Additionally, a microscopic characterization technique is used to explore the effects of GO on the C-A-S-H gel microstructure, interface characteristics, and pore structure of the cement paste of UHPC. Finally, molecular dynamics simulation is utilized to further analyze how GO enhances the performance of abrasion-resistant UHPC. This research will provide novel solutions for the preparation and application of abrasion-resistant ultra-high-performance concrete (UHPC), holding significant importance for advancing concrete technology.

2. Experiment

2.1. Main Raw Materials

(1) Cement: based on our team's relevant research of iron-rich phase silicate cement [36,37], a novel industrial-scale cement with an iron-rich phase (HFC1) was produced by Guangxi Yufeng Cement Co., Ltd. (Guigang, China) through a secondary grinding process. HFC1 has a high corrosion resistance and abrasion resistance (Tables 1 and 2).

Table 1. The main chemical compositions of HFC1/%.

Type	SiO_2	Al_2O_3	Fe_2O_3	MgO	CaO	Na_2O	K_2O	SO_3	TiO_2	P_2O_5	Loss
HFC1	21.61	3.14	6.17	1.98	62.32	0.16	0.37	2.16	0.23	0.14	1.72

Table 2. The main performance indexes of HFC1.

Type	Specific Surface Area/(cm^2/g)	Initial Setting Time/min	3-Day Compressive Strength/MPa	28-Day Compressive Strength/MPa
HFC1	3580	195	25.8	59.3

(2) Fly ash microspheres (FAMs): FAMs were produced by Tianjin Zhucheng New Material Co. (Tianjin, China). They have a specific surface area exceeding 1200 m^2/kg, and their 28-day activity index is greater than 90%. Table 3 presents the physical performance indexes.

Table 3. Physical performance indexes of FAM.

Appearance	Spherical Density	Bulk Density	Thixotropic Index	Crystal Structure
Spherality	2.50 g/cm^3	0.65 g/cm^3	7.6	Amorphous

(3) Silica fume (SF): SF was produced by Shanghai Tiankai Company (Shanghai, China), with a specific surface area of 19,500 m^2/kg and a SiO_2 content of 96.3%, its main chemical composition is shown in Table 4.

Table 4. Main chemical compositions of SF/%.

Oxide	SiO_2	Al_2O_3	Fe_2O_3	CaO	MgO	SO_3	K_2O	Na_2O	Loss
SF	96.34	0.61	0.16	0.54	0.25	0.13	0.21	0.08	1.68

(4) High-titanium heavy slag sand (HTHSS): Produced by Panzhihua Huanye Metallurgical Slag Development Co. (Panzhihua, China), it has an apparent density of 3100 kg/m³ and a fineness modulus of 3.0. The results of the X-ray fluorescence physical analysis are presented in Table 5, while the physical properties are shown in Table 6.

Table 5. Main chemical compositions of HTHSS/%.

Oxide	SiO_2	Al_2O_3	Fe_2O_3	CaO	MgO	TiO_2	FeO	mFe	Loss
HTHSS	18.09	14.85	5.31	24.65	8.50	22.65	2.55	2.12	1.28

Table 6. Physical property parameters of HTHSS.

Apparent Density/(kg/m³)	Stone Powder Content/%	Water Absorption/%	Crushing Index/%	Fineness Modulus
3100	5.0	10.1	5.3	3.0

(5) Rubber particles (RPs): These are broken RPs from waste tires with a particle size of 1–3 mm and an apparent density of 1120 kg/m³. They are produced by Dujiangyan Huayi Rubber Co. (Dujiangyan, China). The surface of the RPs was modified with dopamine hydrochloride PDA (Aladdin, Shanghai, China, D103111) (Table 7).

Table 7. Modification methods of RP.

Modification Methods	Main Steps
PDA	The RPs were treated with a 5% NaOH solution for 30 min, followed by soaking a 5% potassium permanganate solution for another 30 min. Finally, they were soaked in a dopamine solution with a concentration of 2 mg/mL for an additional 30 min.

(6) Fibers: there are a total of three types of fibers used—microfine copper-plated steel fibers, multi-anchor steel fibers, and heat-shrinkable fibers [40], which are characterized by the following specifications (Table 8).

Table 8. The main performance indicators of fibers.

Indicators	Microfine Coppe-Plated Steel Fibers	Microfine Coppe-Plated Steel Fibers	Heat-Shrinkable Fibers
Type	CW01-02/06	CW07-09/60	-
Appearance	monofilament	both ends with end hooks	-
Elastic modulus/GPa	200~220	210~230	-
Nominal length/mm	13	20	12
Equivalent diameter/mm	0.25	0.5	2dtex
Fracture strength/MPa	≥2200	≥1000	cn/dtex ≥ 12
Elongation rate at breaking/%	≥10	≥10	6–8

(7) Water-reducing agent: polycarboxylate superplasticizer (PCE) for UHPC, containing 35% solid content and achieving a water reduction rate of 35%.

(8) Graphene oxide (GO): GO was provided by Nanjing Xianfeng Nanomaterials Science and Technology Co. (Nanjing, China). The main size distribution range of the GO nanoplatelets was 50–200 nm, and their average thickness was 0.8–1.2 nm, with good dispersibility. The main technical parameters and indicators are shown in Table 9.

Table 9. Main technical parameters of GO.

Purity	Concentration (mg/mL)	pH	Carbon Content (%)	Oxygen Content (%)
99 wt.%	1.0	7.6	51–62	38–47

2.2. Test Method

(1) Workability

According to the relevant requirements of 'Standard for Test Methods of Performance on Ordinary Fresh Concrete' (GB/T 50080-2016) [41], extensibility is measured using a steel base plate with a minimum size of 1500 mm × 1500 mm and a thickness of at least 3 mm, with maximum deflection not exceeding 3 mm. If the difference between the two diameter measurements is less than 50 mm, the average is used as the test result; if the difference is 50 mm or more, resampling is required.

(2) Compressive and Flexural Strength

According to the relevant provisions of the Standard for Test Methods of Concrete Physical and Mechanical Properties (GB/T 50081-2019) [42], the compressive strength test should use a 100 mm × 100 mm × 100 mm cube specimen with a loading rate of 1.2 MPa/s to 1.4 MPa/s; the flexural strength test should use a 100 mm × 100 mm × 400 mm prism specimen with a loading rate of 0.08 MPa/s to 0.1 MPa/s.

(3) Abrasion Resistance

According to the Test Code for Hydraulic Concrete (SL352-2006) [43], the "Underwater Steel Ball Method" is used to test the abrasion resistance of ultra-high-performance concrete. The advantage of the underwater steel ball method lies in its simple specimen preparation and its ability to effectively simulate the abrasive wear caused by sand and gravel in flowing water, measuring the relative resistance of the concrete surface to abrasion under high-speed underwater flow. Abrasion resistance is expressed in terms of abrasion resistance or abrasion wear rate. The testing instrument used is the SJA-1 Concrete Abrasion Resistance (Underwater Steel Ball Method) tester, and the testing instrument and specimen are shown in Figure 1. The specimen dimensions are Φ300 mm × h100 mm, with an impeller rotation speed of 1200 r/min.

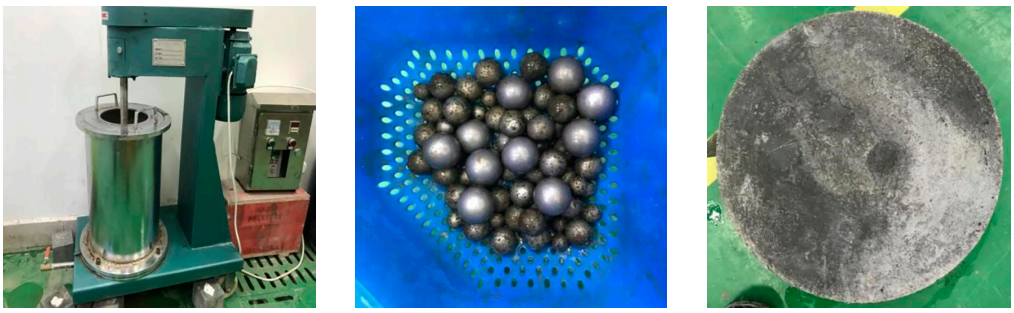

Figure 1. Abrasion Testing Equipment and Specimen (Underwater Steel Ball Method).

(4) Impact Resistance

As stipulated by US ACI544-2R-89 [44], the "Hammer Impact Method" was employed to assess the impact resistance of the UHPC. A 2.5 kg hammer was utilized to impact the concrete specimens by freely dropping on a 63 mm diameter ball on a platform from a height of 0.4 m until the specimens exhibited a final cracked state. The testing instrument is a CSK-VI multifunctional electric compactor manufactured by the Beijing Zhongke Luda Testing Instrument Co, Beijing, China. The impact-resistant specimen has dimensions of 100 mm in diameter by 50 mm in height (Figure 2).

Figure 2. Impact test instrument (falling weight impact method).

(5) Microscopic Characterization Technique

The ^29Si and ^27Al NMR spectral tests were conducted using a Bruker solid-state NMR spectrometer from Germany. The MAS probes used were 4 mm and 7 mm, with resonance frequencies of 79.3 MHz and 104 MHz, pulse widths of 4 μs and 0.5 μs, repetition times of 5 s and 2 s, respectively, and a total of 1024 scans.

The phase composition of different cement pastes was tested using a D/MAX-IIIA X-ray diffractometer from Japan's RIGAKU company (Tokyo, Japan). The Cu(Kα) radiation source had a rated power of 4 kW and a working current of 60 mA. The scan step size was 0.02°, with a scan range from 5° to 70°.

The pore structure of the UHPC cement paste was tested using the BET nitrogen adsorption method with the TriStar II 3020 multi-channel specific surface area and pore size analyzer from Micromeritics, Norcross, GA, USA. The BET specific surface area analysis employed the Langmuir surface area model with a resolution down to 0.01 m^2/g, while pore size distribution analysis used the Dubinin–Radushkevich micropore model, covering a range of 2 nm to 300 nm.

The interfacial transition zone (ITZ) between the rubber particles and the UHPC cement paste was characterized in terms of microhardness, hydration product accumulation, and microstructure. A cutting machine was used to prepare UHPC samples aged to the specified period, which included rubber particles, ITZ, and cement matrix. The samples were polished to a mirror finish with a metallographic polisher, and the microhardness was measured using the HVS-1000 digital microhardness tester from Shanghai Lianer Testing Equipment Co., Ltd. (Shanghai, China). The Vickers diamond indenter with a 136° apex angle was used for the tests. The microhardness is defined as the ratio of applied load to the indentation surface area, as shown in Equation (1).

$$HV = \frac{2P\sin(136°/2)}{D^2} \times 9.8 \quad (1)$$

In the formula, HV represents the Vickers microhardness of the specimen, measured in MPa; P is the applied load in kgf; and D is the average length of the indentation diagonal in mm.

2.3. Design of Proportions

Based on the results of the previous research [17], the basic mix proportions for the comparison test between unincorporated and incorporated GO were designed, and the specific mixing proportions are shown in Table 10.

Table 10. Mix proportion.

Number	Water Binder Ratio	Raw Materials/(kg/m³)				PCE	RP/ vol%	Fibers/vol%	GO/%
		HFC1	SF	FAM	HTHSS				
#19	0.17	800	200	150	1150	3.1%	10	2.6	/
#22	0.17	800	200	150	1150	3.1%	10	2.6	0.03

Note: 2.0 vol% copper-plated steel fibers, 0.5 vol% multi-anchor steel fibers, and a 0.1 vol% heat-shrinkable fiber blend were used.

3. Results and Discussion

3.1. Effect of GO on the Macroscopic Properties of UHPC

According to the reference mix proportion presented in Table 10, the experiment investigated the effects of GO on the impact and abrasion macroscopic properties of UHPC. The corresponding results are illustrated in Table 11 and Figure 3. It can be observed that incorporating an appropriate amount of GO into abrasion-resistant UHPC has a negligible impact on its workability, while significantly enhancing its mechanical properties, abrasion resistance, and impact resistance. This improvement can be attributed to the uniform dispersion of GO within the UHPC matrix, which acts as a template effect and facilitates assembly during the hydration process of UHPC cementitious materials [45]. Consequently, this optimization greatly enhances the interface structure and increases the hydration degree. Furthermore, uniformly dispersed GO primarily consists of single-layered sheets that react with cement-based materials [46], thereby impeding crack propagation, reinforcing weak regions, and improving paste toughness.

Table 11. Test results of the effect of GO on UHPC performance.

Number	Slump /mm	Slump-Flow /mm	28d Flexural Tensile Strength/MPa	28d Compressive Strength/MPa	28d Abrasion Resistance /h × (kg/m²)⁻¹	Final Crack Impact Energy/kJ
#19	250	645	26.5	149.8	169	170
#22	240	635	27.3	152.5	172	173

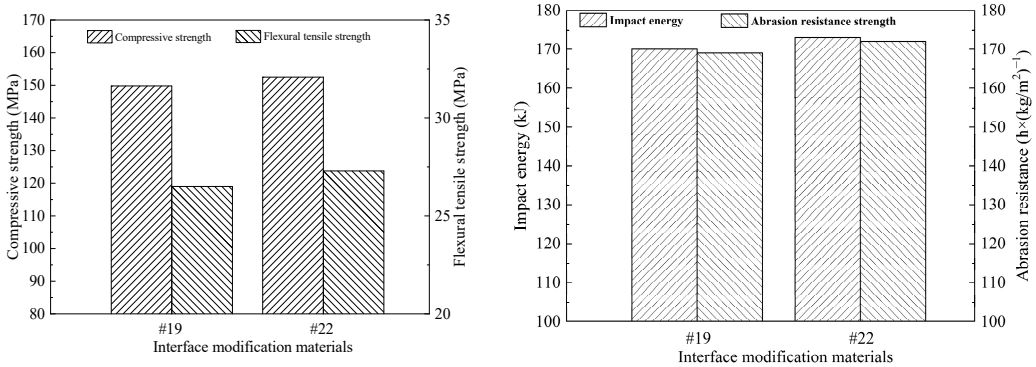

Figure 3. The effect of GO on the performance of UHPC.

3.2. Effect of GO on the Microstructure of UHPC

3.2.1. Effect on the Microstructure of UHPC Cementitious Paste

To study the effect of GO on the microstructure of UHPC cementitious paste, the 29Si NMR spectra of cementitious paste externally doped with 3% GO (diluted 100 times) are presented in Figure 4, and the results of its deconvolution are shown in Table 12. This table reveals that the hydration degree of the paste doped with GO is greater than that of the undoped one. This is primarily due to the large specific surface area of GO, which

provides nucleation sites for the hydration of cement and promotes hydration. Furthermore, GO exerts a small-scale effect on cementitious pastes [37,47,48], and the incorporation of GO significantly improves the internal microstructure of the paste, which further enhances the degree of hydration of the paste. The alterations in MCL and Al [4]/Si with the incorporation of GO are not obvious, suggesting that GO does not induce modifications in the silicon–oxygen chain of the C-A-S-H gel of cementitious pastes.

Table 12. Deconvolution results of 29Si NMR spectra of UHPC doped with GO.

Group	Q^n Relative Intensity Value I/%							α_C/%	MCL	Al [4]/Si
	Q^0	Q^{0H}	Q^1	Q^2(1Al)	Q^{2B}	Q^{2P}	$Q^3 + Q^4$			
A1	34.24	5.44	5.11	3.14	3.36	4.57	44.14	29.05	6.95	0.097
A2	31.25	9.79	8.68	5.18	9.44	4.06	31.60	35.25	6.90	0.095

Note: A1 and A2 are undoped GO and GO-doped cementitious pastes, respectively.

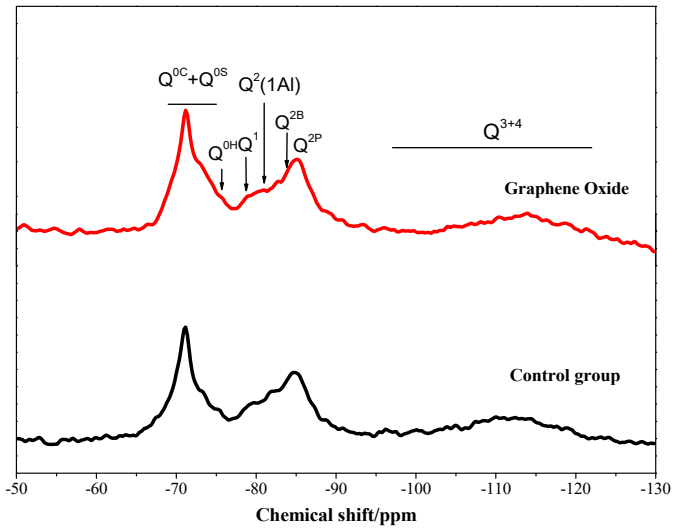

Figure 4. 29Si NMR spectra of UHPC doped with GO.

3.2.2. Effect on the Aggregate–Paste Interface in UHPC

To study the influence of GO doping on the aggregate–paste interface in UHPC, microhardness analysis was conducted on the HTHSS–paste interface of two groups of UHPCs. The results are shown in Figure 5. B1 represents UHPC without GO doping, while B2 represents UHPC with GO doping.

As illustrated in Figure 5, the microhardness of the interface transition zone gradually decreases with increasing distance from the surface of the pre-wetted HTHSS. This is primarily due to the gradual release of water from the pre-wetted porous HTHSS after the hardening of the cementitious paste, which leads to an increase in the degree of hydration of the cementitious paste at the interface. As the distance from the surface of the HTHSS increases, the water transfer effect becomes less pronounced, resulting in a reduction in microhardness. The incorporation of GO into UHPC has been observed to enhance the microhardness of the transition zone at the interface of HTHSS-paste at the same distance, while simultaneously improving the transition zone at the interface of UHPC.

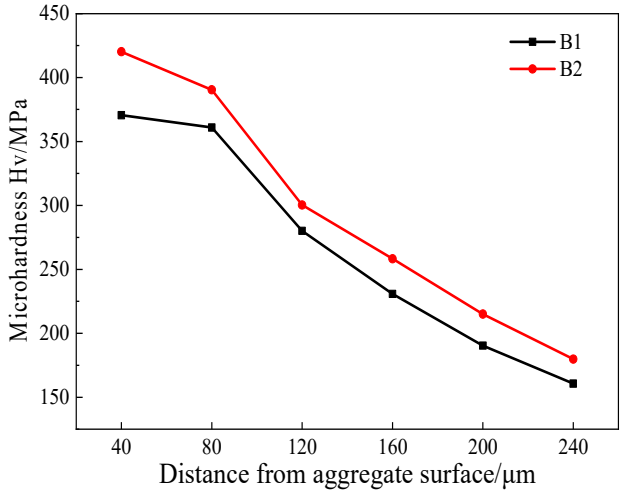

Figure 5. The changing trend of microhardness in the transition zone of the HTHSS-paste interface.

3.2.3. Effect on the Pore Structure of UHPC

Figure 6 illustrates the impact of GO on the pore structure of UHPC cementitious paste, while Table 13 presents the pore structure parameters. As shown in the preceding charts, the incorporation of GO into UHPC cementitious paste can markedly enhance the pore structure. Specifically, the average pore size of the pores in UHPC was reduced to 61.83 Å. Additionally, the cumulative pore volume and specific surface area of the pores were also reduced accordingly, and were 15.81 m^2/g and 0.027 mL/g, respectively.

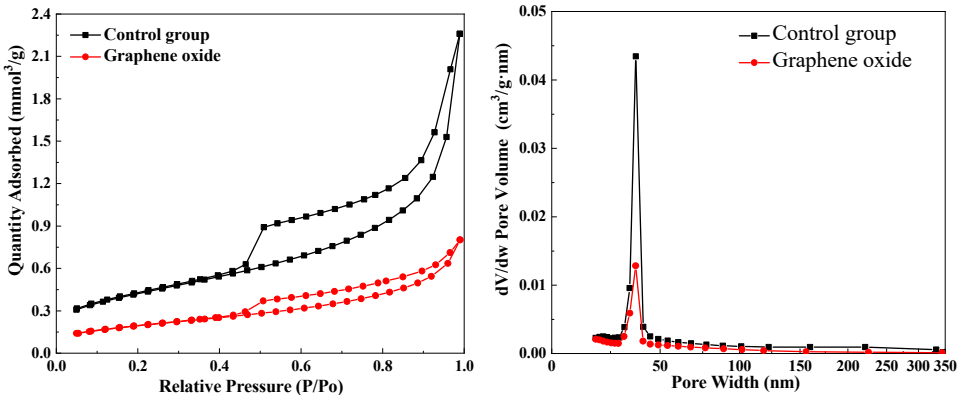

Figure 6. The effect of GO on the pore structure of UHPC (left: N2 adsorption–desorption isotherm, right: N2 desorption pore-size distributions).

Table 13. The pore structure parameters of Figure 6.

Interfacial Modified Material	Specific Surface Area/($m^2 \cdot g^{-1}$)	Cumulative Pore Volume/(mL·g^{-1})	Average Pore Size/Å
Undoped	33.87	0.078	75.64
GO	15.81	0.027	61.83

3.3. Molecular Dynamics Simulation of GO to Enhance the Performance of Abrasion-Resistance UHPC

3.3.1. Molecular Model of UHPC

Calcium silicoaluminate hydrate (C-A-S-H) serves as the main hydration product in UHPC [49]. To explore the mechanisms of abrasion resistance and microstructural evolution in UHPC under abrasion and erosion, a molecular model of C-A-S-H was created, as

depicted in Figure 7. The modeling process involved the following steps: First, the 11 Å Torbay mullite model by Hamid was utilized as the initial model [50], and all water molecules were removed to obtain a dry model of the calcium–silicon skeleton. To achieve a C-S-H model with a Ca/Si ratio of 2.15, the bridging silica–oxygen tetrahedra along the silica–oxygen chains were randomly removed according to experimentally determined Ca/Si and Al/Si ratios, as well as the average molecular chain length (MCL). A C-A-S-H model with an Al/Si ratio of 0.06 was established by introducing aluminum–oxygen polyhedrons onto the defects at the bridging position of the silica–oxygen chains of the C-S-H model to ensure that the parameters of the model, such as Ca/Si ratio, Al/Si ratio, and MCL, conformed to the results of the experimental tests. Table 14 compares the structural parameters of the C-A-S-H molecular model with the experimental results, showing that the constructed model aligns closely with experimental data, confirming its accuracy and consistency with actual conditions. Following this, water molecules were randomly absorbed using the grand canonical Monte Carlo method, while hydrolysis, silica–alumina–oxygen chain breakage, and polymerization reactions in the C-A-S-H structure were simulated via the reactive force field molecular dynamics method. The Monte Carlo simulation was conducted at a chemical potential of 0 eV and a temperature of 300 K, allowing for simulation of the material's water uptake reaction in an ideal, infinitely large container. Molecular dynamics simulations were performed at 300 K and 1 atmosphere pressure. Figure 7 shows the developed C-S-H and C-A-S-H models. The cell parameters of the C-S-H model are a = 20.94 Å, b = 23.01 Å, c = 21.37 Å, α = 90°, β = 90°, and γ = 90°. The cell parameters of the C-A-S-H model are a = 21.04 Å, b = 22.92 Å, c = 21.39 Å, α = 90°, β = 90°, and γ = 90°.

Table 14. Comparisons of parameters of C-A-S-H model with experimental results.

Parameters	Ca/Si	Al/Si	MCL
Experimental value	2.0–2.4	0.05–0.10	5.0–10.0
Simulation value	2.15	0.06	6.0

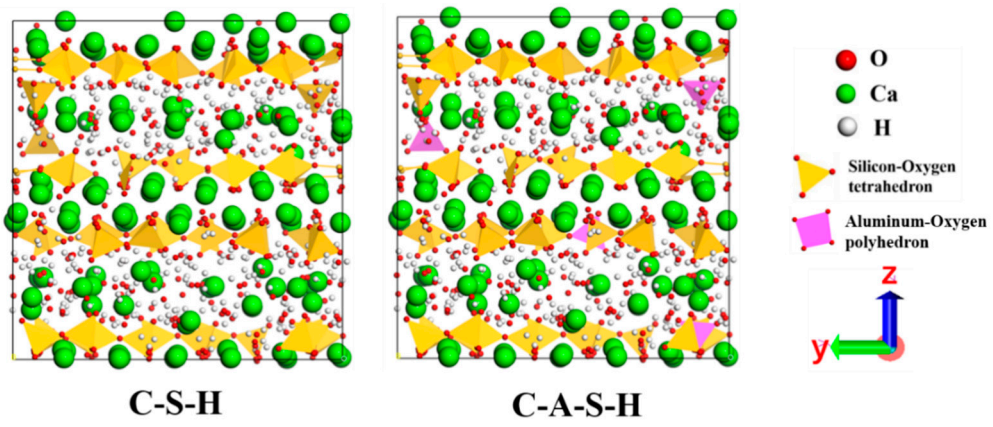

Figure 7. Constructed C-S-H and C-A-S-H molecular models.

3.3.2. The Abrasion Resistance Model of UHPC

Simulating the macroscopic effects of bed load materials like mud, sand, and stones on UHPC's abrasion resistance is not feasible at the molecular scale. Thus, to examine UHPC's abrasion resistance on a molecular level, water molecules were used as impactors to represent the abrasion resistance of the microstructure of UHPC cementitious paste against bed load materials. This was achieved by constructing the UHPC abrasion resistance model, which consists of two parts, namely, the C-A-S-H and the water molecules. As illustrated in Figure 8, the C-A-S-H model was initially generated through the aforementioned methodology. Subsequently, a supercell extension was performed to reveal the

interlayer region of the model, resulting in a C-A-S-H model with dimensions of 42.08 Å × 45.84 Å × 17 Å. A water molecule layer of 42.08 Å × 45.84 Å × 20 Å was constructed by employing the Monte Carlo water absorption method to a saturated solution state (~1 g/cm^3) and was positioned on top of the C-A-S-H model. To minimize the error of boundary effects on the model, periodic boundaries were set in the X, Y, and Z directions. A vacuum layer of a specified thickness was established above the water molecules to preclude their interaction with the underlying C-A-S-H substrate, which was subjected to periodic boundary conditions. The final parameters of the entire model are a = 42.08 Å, b = 45.84 Å, c = 50.92 Å, α = 90°, β = 90°, and γ = 90°. The entire simulation process was conducted using the LAMMPS software (version 2 Aug 2023). The system was maintained in an NVT state, with a temperature of 300 K. The integration of the atom trajectories into the current simulation was performed using the Verlet algorithm, with a time step of 0.25 fs. During the simulation process, the system was first equilibrated for 100 ps to ensure full interaction between the water molecules and the C-A-S-H substrate, reaching a thermodynamic equilibrium state. Subsequently, an elastic force was then applied to the Ca atoms in the lowest layer of the C-A-S-H substrate to maintain its stability. At the same time, a force in the Y-direction was applied to the water molecules in the upper layer to simulate the abrasion test of UHPC. The force applied was 0.5 Kcal/mol·Å. The abrasion process was completed within 100 ps, during which atom trajectory data were collected.

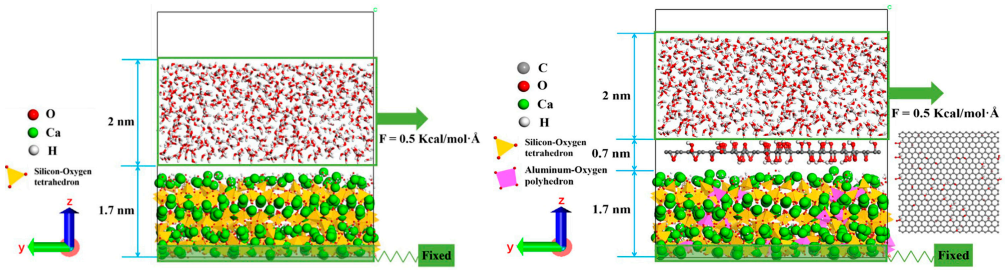

(**a**) (**b**)

Figure 8. (**a**) Constructed abrasion resistance C-A-S-H molecular model. (**b**) Constructed abrasion resistance C-A-S-H/GO molecular model.

The experimental results demonstrated that the incorporation of GO would enhance the abrasion resistance of UHPC, leading to the construction of the C-A-S-H/GO molecular model to elucidate the underlying microscopic mechanism through molecular dynamics simulations. The C-A-S-H/GO molecular model was constructed using the following method: first, a molecular model was created for 4 nm × 4 nm graphene. Then, hydroxyl (-OH) and epoxide (OO) functional groups were randomly added to the surface of the graphene, and carboxyl (-COOH) functional groups were randomly added at the boundary of the graphene, with a total coverage of 20%. The constructed GO molecular model was then positioned between the water molecule layer and the C-A-S-H substrate, thereby forming the C-A-S-H/GO model. A thermodynamic equilibrium of 100 ps was initially conducted to ensure a complete reaction and equilibrium between the C-A-S-H, GO, and water molecule layers. Subsequently, an abrasion resistance simulation was conducted. The specific simulation processes are identical to those previously described. Figure 8 depicts the constructed abrasion resistance C-A-S-H/GO model.

3.3.3. Molecular Dynamics Reactive Force Field

Molecular dynamics simulations of UHPC were carried out using a reactive force field (Reaxff) [51]. In Reaxff, the formation and breaking of chemical bonds depends on the atomic spacing and bond order at each moment. The chemical bonds between atoms are determined by their positions, after which charges and bond orders for the atoms are calculated. This differs from the force fields typically employed for concrete, such as Clayff and

CSHFF. Moreover, Reaxff integrates the advantages of quantum mechanics and empirical force fields to provide an accurate representation of chemical reactions during the simulation process. Currently, Reaxff is a commonly used tool for modeling C-S-H properties. The force field parameters for individual atoms can be derived from previous studies [52,53].

3.3.4. Effect of GO on Abrasion Resistance of UHPC

Figure 9 presents the results of the C-A-S-H/GO model's resistance to abrasion during a 100 ps water flow impact. Figure 9a illustrates that the average displacements of the atoms Ca, Si, Al, and Os exhibit a comparable trend and reach a stable value of approximately 0.13 Å under abrasion by water flow. This result is considerably smaller than that observed in the C-A-S-H model. Similarly, Figure 9b demonstrates that the average displacements of Ow and Hw are stabilized at approximately 0.1 Å after the addition of GO molecules. As illustrated in Figure 9c, the average displacements of O_water and H_water also demonstrate a linear increase under the influence of water flow. The average displacements of both O_water and H_water reach 1600 Å at 100 ps, which is considerably larger than the 1377 Å observed in the C-A-S-H model. Furthermore, as depicted in Figure 9d, the average displacements of GO are also remarkably stable. All these results indicate that the doping of GO improves the abrasion resistance of UHPC.

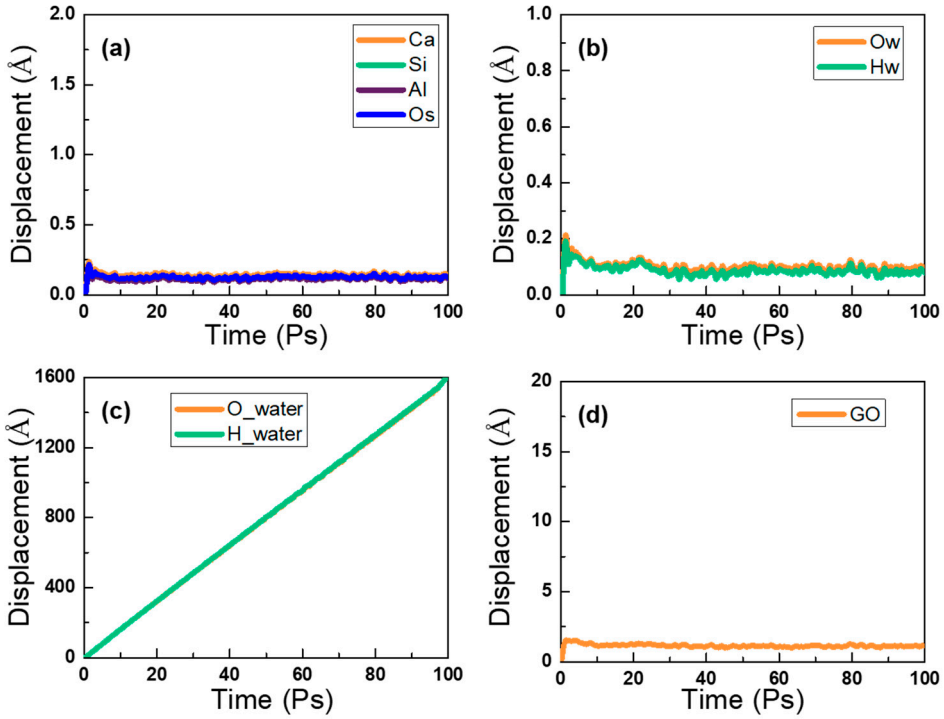

Figure 9. The average displacement of atoms in the C-A-S-H/GO model under abrasion.

To interpret the above results, the RDF results (Figure 10) of the two models C-A-S-H and C-A-S-H/GO are compared. As illustrated in Figure 10a, the peak of the RDF between Ca-O_water in the C-A-S-H/GO model is significantly diminished due to GO, and the chemical bonding is notably weak. Furthermore, Figure 10b shows that, unlike the C-A-S-H model, there is no noticeable interaction between the water flow and the substrate. Consequently, the abrasion effect of the water flow has minimal impact on the C-A-S-H substrate, thereby enhancing the abrasion resistance of C-A-S-H.

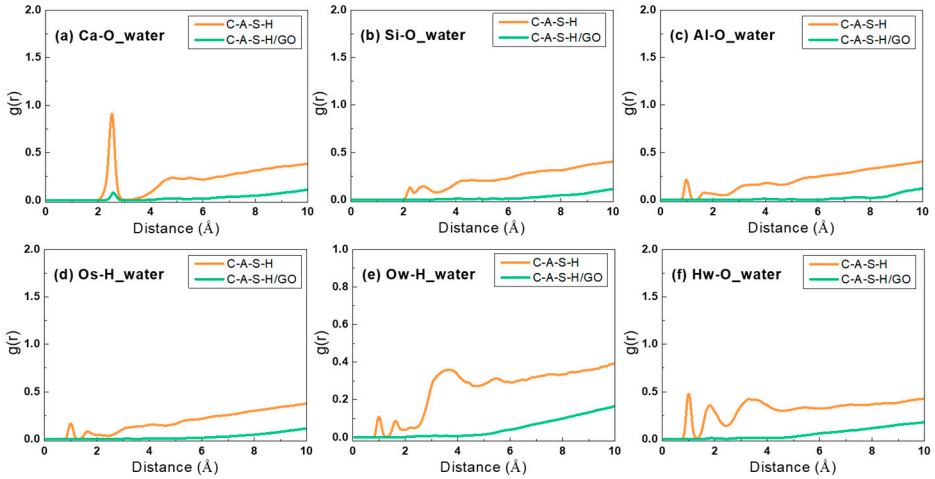

Figure 10. RDF between water flow and substrate: comparisons of C-A-S-H and C-A-S-H/GO model.

Figure 11 illustrates the results of the RDF analysis concerning the chemical bond formation between GO and the C-A-S-H substrate in the C-A-S-H/GO model. As shown in Figure 11, both the O and H on the GO formed chemical bonds with individual atoms of the C-A-S-H substrate, including Ca-O, Al-O ionic bonds, and hydrogen bonds. The strength of these chemical bond interactions was significant, suggesting that GO was firmly attached to the C-A-S-H substrate through these interactions, thereby stabilizing the connection. Figure 12 illustrates the results of the RDF analysis between GO molecules and water flow. It can be observed that some spatial interactions were formed between the O and H atoms in the water flow and GO. However, despite these interactions with the water flow, the GO remained stably connected to the C-A-S-H substrate, with an extremely small displacement value. This indicates that the doping of GO improved the abrasion resistance of C-A-S-H.

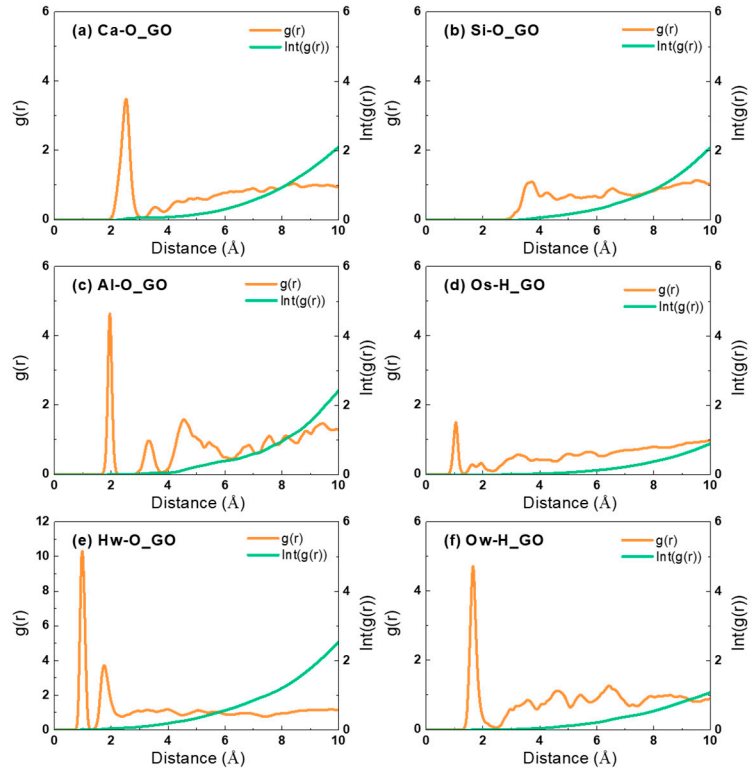

Figure 11. RDF between GO and C-A-S-H substrate.

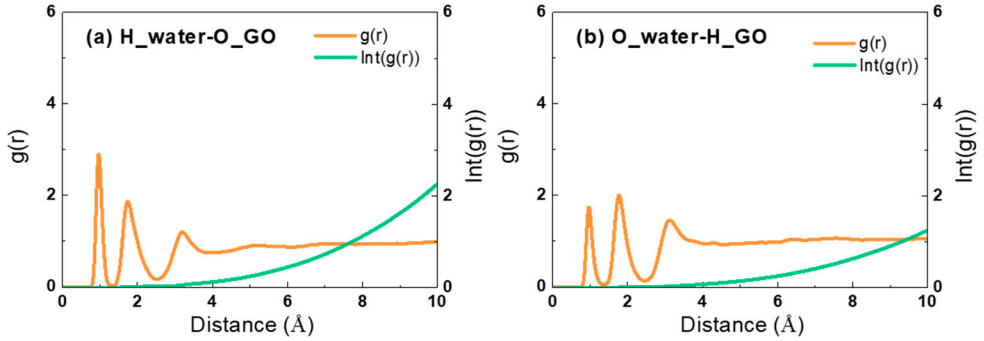

Figure 12. RDF between GO and water flow.

4. Conclusions

(1) The incorporation of an appropriate amount of GO does not significantly affect the working performance of abrasion-resistant UHPC, but rather enhances its mechanical properties, abrasion resistance, and impact resistance. This is because GO has a high surface area and good lubrication properties. When mixed in moderate quantities, GO does not significantly increase the viscosity of the concrete, which means that the concrete can still maintain good workability.

(2) The hydration degree of the abrasion-resistant UHPC paste doped with an appropriate amount of GO was found to be higher than that of the un-doped paste. However, this did not result in any alteration to the silicon–oxygen chain of the C-A-S-H gel present in the cementitious paste. Additionally, the incorporation of GO can refine the pore structure of the UHPC cementitious paste and improve the microstructure of the transition zone at the interface between the aggregate and the cementitious paste.

(3) GO primarily enhances the impact resistance of UHPC by increasing the hydration degree of the UHPC matrix, improving the pore structure and interfacial structure of UHPC, and achieving the toughening of UHPC cementitious paste. In addition, the incorporation of GO with hybrid fibers and modified rubber particles can achieve the multi-scale toughening of abrasion-resistant UHPC, significantly enhancing the impact resistance of UHPC materials.

(4) Molecular dynamics simulations have demonstrated that both the O and H on GO form extremely strong chemical bonds with the atoms of the C-A-S-H substrate, including Ca-O, Al-O ionic bonds, and hydrogen bonds. The strong and stable chemical bonding interactions between GO and the C-A-S-H substrate result in a significant improvement in the abrasion resistance of C-A-S-H.

(5) Although the incorporation of graphene oxide (GO) can enhance certain properties of ultra-high-performance concrete (UHPC) to some extent, the synergistic effects between GO and other reinforcement materials remain underexplored. For example, the toughening mechanisms arising from the synergy between GO and multiscale reinforcement materials such as modified rubber particles, or the enhancement of interfacial bonding through the hybridization of GO with carbon fibers and carbon nanotubes to optimize the microstructure, are yet to be studied. These emerging research directions could provide theoretical support for developing high-performance, multiscale-reinforced UHPC materials.

Author Contributions: Methodology, data curation, and writing—original draft, T.H.; methodology and data curation, W.X. (Wei Xie); methodology and data curation, F.W.; methodology and data curation, Z.Y.; methodology and data curation, F.X.; methodology and writing—review and editing, J.L.; methodology and data curation, Y.D.; methodology and writing—review and editing, Q.D.; methodology and data curation, Y.H.; methodology and data curation, W.X. (Wei Xu); methodology and data curation, H.Y. All authors have read and agreed to the published version of the manuscript.

Funding: The research was supported by the Open Fund (SYSJJ2023-13) of the State Key Laboratory of Silicate Materials for Architectures (Wuhan University of Technology). The research was supported by the National Natural Science Foundation of China (52278274). This study was supported by the OpenState Key Laboratory of New Textile Materials and Advanced Processing Technologies. Financial support from Application Foundation Frontier Project of Wuhan Science and Technology Bureau (2022013988065200) was gratefully acknowledged. The research was also supported by the Fundamental and Applied Basic Research Funds of Guangdong Province (2022A1515010508; 2023A1515012753) and the Shaoguan College of Chemical and Civil Engineering.

Institutional Review Board Statement: Not applicable.

Informed Consent Statement: Not applicable.

Data Availability Statement: The data presented in this study are available on request from the corresponding author.

Conflicts of Interest: Feng Wang is employed by Guangdong Gezhouba Zhao Ming Expressway Co., Ltd. The remaining authors declare that the research was conducted in the absence of any commercial or financial relationships that could be construed as a potential conflict of interest.

References

1. He, Z. The coupling effect of concrete abrasion-erosion and other environmental factors. *J. Hydraul. Eng.* **2015**, *46*, 138–145.
2. Peng, E. Study on Wear Properties of Materials' Cavitations Erosion in Fluid with Sand; China Academy of Machinery Science and Technology: Beijing, China, 2006.
3. Xue, J.; Briseghella, B.; Huang, F.; Nuti, C.; Tabatabai, H.; Chen, B. Review of ultra-high performance concrete and its application in bridge engineering. *Constr. Build. Mater.* **2020**, *260*, 119844.
4. Pyo, S.; Abate, S.Y.; Kim, H.K. Abrasion resistance of ultra high performance concrete incorporating coarser aggregate. *Constr. Build. Mater.* **2018**, *165*, 11–16.
5. Hannawi, K.; Bian, H.; Prince-Agbodjan, W.; Raghavan, B. Effect of different types of fibers on the microstructure and the mechanical behavior of Ultra-High Performance Fiber-Reinforced Concretes. *Compos. Part B Eng.* **2016**, *86*, 214–220.
6. Kim, J.J.; Yoo, D.Y. Effects of fiber shape and distance on the pullout behavior of steel fibers embedded in ultra-high-performance concrete. *Cem. Concr. Compos.* **2019**, *103*, 213–223.
7. Xiao, Q.-Q.; Huang, Z.-X.; Zu, X.; Jia, X.; Zhu, Q.-F.; Cai, W. Shaped charge penetration into high- and ultrahigh-strength Steel-Fiber reactive powder concrete targets. *Def. Technol.* **2020**, *16*, 217–224.
8. Wu, Z.; Shi, C.; He, W.; Wu, L. Effects of steel fiber content and shape on mechanical properties of ultra high performance concrete. *Constr. Build. Mater.* **2016**, *103*, 8–14.
9. Yoo, D.-Y.; Kim, S.; Kim, J.-J.; Chun, B. An experimental study on pullout and tensile behavior of ultra-high-performance concrete reinforced with various steel fibers. *Constr. Build. Mater.* **2019**, *206*, 46–61.
10. Zhang, W.; Zhang, Z.; Liu, P.; Zhang, Y.; Zhang, C.; She, W. Uniaxial Tensile and Compressive Stress-Strain Behavior of Multi-scale Fiber-reinforced Ultra-high Performance Concrete. *J. Chin. Ceram. Soc.* **2020**, *48*, 1155–1166.
11. Chun, B.; Yoo, D.Y. Hybrid effect of macro and micro steel fibers on the pullout and tensile behaviors of ultra-high-performance concrete. *Compos. Part B Eng.* **2019**, *162*, 344–360.
12. Zhang, G.; Ge, J.; Ding, Q.; Yang, J.; Xiang, W.; Hu, J. Preparation and Formation Mechanism of Lightweight Ultra-High Performance Concrete. *J. Chin. Ceram. Soc.* **2021**, *49*, 381–390.
13. Shao, X.; Fan, W.; Huang, Z. Application of Ultra-High-Performance Concrete in engineering structures. *China Civ. Eng. J.* **2021**, *54*, 1–13.
14. Fan, W.; Shen, D.; Zhang, Z.; Huang, X.; Shao, X. A novel UHPFRC based protective structure for bridge columns against vehicle collisions: Experiment, simulation, and optimization. *Eng. Struct.* **2020**, *207*, 110247.
15. Zhu, Y.; Zhang, Y.; Hussein, H.H.; Chen, G. Flexural strengthening of reinforced concrete beams or slabs using ultra-high performance concrete (UHPC): A state of the art review. *Eng. Struct.* **2020**, *205*, 110035.
16. Ding, Q.; Xiang, W.; Zhang, G.; Hu, C. Effect of Pre-wetting Lightweight Aggregates on the Mechanical Performances and Microstructure of Cement Pastes. *J. Wuhan Univ. Technol. Mater. Sci. Ed.* **2020**, *35*, 140–146.
17. Li, J.; Wang, X.; Chen, D.; Wu, D.; Han, Z.; Hou, D.; Zhen, Z.; Peng, C.; Ding, Q.; Yin, B. Design and application of UHPC with high abrasion resistance. *Constr. Build. Mater.* **2021**, *309*, 125141.
18. Li, J.; Yu, Z.; Xu, F.; Guo, Z.; Ding, Q.; Hou, D. The evolution mechanism of abrasion-resistance UHPC microstructure under impact and erosion. *Constr. Build. Mater.* **2024**, *411*, 134282.
19. Chu, H.; Gao, L.; Qin, J.; Tang, J.; Jiang, J. Effects of Graphene Sulfonate Nanosheets on Mechanical Properties and Durability of Ultra-high Performance Concrete Produced by Recycled Sand. *Mater. Rep.* **2022**, *36*, 95–99.
20. Wang, Y.; Ang, J.; Ouyang, D. Effect of graphene oxide on mechanical properties of cement mortar and its strengthening mechanism. *Materials* **2019**, *12*, 37–53.

21. Lu, L.; Ouyang, D. Properties of cement mortar and ultra-high strength concrete incorporating graphene oxide nanosheets. *Nanomaterials* **2017**, *7*, 187–201.
22. Devi, S.C.; Khan, R.A. Effect of graphene oxide on mechanical and durability performance of concrete. *J. Build. Eng.* **2020**, *27*, 101007.
23. Gui, C.; Xu, Z.; Jiang, Y.; Li, S. Preparation of graphene oxide/recycled cement-based composite materials. *Acta Mater. Compos. Sin.* **2021**, *38*, 1526–1534.
24. Du, M.; Zhang, G. Progress in preparation and application of graphene. *Inorg. Chem. Ind.* **2019**, *51*, 12–15.
25. Yu, L.; Wu, R. Using graphene oxide to improve the properties of ultra-high-performance concrete with fine recycled aggregate. *Constr. Build. Mater.* **2020**, *259*, 120657.
26. Chu, H.; Zhang, Y.; Wang, F.; Feng, T.; Wang, L.; Wang, D. Effect of graphene oxide on mechanical properties and durability of ultra-high-performance concrete prepared from recycled sand. *Nanomaterials* **2020**, *10*, 1718.
27. Kumar, T.N.; Vardhan, K.V.; Krishna, M.H.; Nagaraja, P.V. Effect of Graphene Oxide Dispersion Method on Properties of Cement-based Materials. *J. Chin. Ceram. Soc.* **2020**, *39*, 677–684.
28. Xie, X.-L.; Mai, Y.-W.; Zhou, X.-P. Dispersion and alignment of carbon nanotubes in polymer matrix: A review. *Mater. Sci. Eng. R Rep.* **2005**, *49*, 89–112.
29. Odegard, G.; Gates, T.; Wise, K.; Park, C.; Siochi, E. Constitutive modeling of nanotube-reinforced polymer composites. Compos. *Sci. Technol.* **2003**, *63*, 1671–1687.
30. Lu, S.; Cui, Y.; Sun, T.; Zhao, H.-F.; Liu, J.-J.; Ding, H.-D. Effect of graphene oxide on fluidity of cement paste and structure and properties of cement stone. *J. Funct. Mater.* **2015**, *46*, 4051–4056.
31. Lu, S.; Luo, X.; Zhang, J.; Gao, D.; Sun, L.; Hu, H. Graphene Oxide Controlled Cement Materials Formation of Large-scale Ordered Structure and Its Properties Characterization. *Mater. Rep.* **2017**, *31*, 10–14.
32. Zhang, D.; Liang, Y. Effect of graphene oxide on macro mechanical properties and hydration process of cement. *Concrete* **2019**, 37–41+48.
33. Saafi, M.; Tang, L.; Fung, J.; Rahman, M.; Liggat, J. Enhanced properties of graphene/fly ash geopolymeric composite cement. C*ement Concr. Res.* **2015**, *67*, 292–299.
34. Ranjbar, N.; Mehrali, M.; Mehrali, M.; Alengaram, U.J.; Jumaat, M.Z. Graphene nanoplatelet-fly ash based geopolymer composites. *Cem. Concr. Res.* **2015**, *76*, 222–231.
35. Lu, S.; Liu, J.; Qiu, C.; Ma, Y.; Zhou, Q. Microstructure and mechanism of nano-graphene oxide reinforced and toughened cement-based composites. *J. Funct. Mater.* **2014**, *45*, 4084–4089.
36. Yang, L.; Yuan, X. Study on mechanical properties of cement mortar enhanced by graphene oxide mixed with graphene and its mechanism. *J. Funct. Mater.* **2019**, 50, *12089*–12096.
37. Meng, W.; Khayat, K.H. Mechanical properties of ultra-high-performance concrete enhanced with graphite nanoplatelets and carbon nanofibers. *Compos. B* **2016**, *107*, 113–122.
38. Meng, W.; Khayat, K.H. Effect of graphite nanoplatelets and carbon nanofibers on rheology, hydration, shrinkage, mechanical properties and microstructure of UHPC. *Cem. Concr.* **2018**, *105*, 64–71.
39. Ren, Z. Study on Properties of Ultra High Performance Cement-Based Materials Modified by Graphene Oxide; Wuhan University of Technology: Wuhan, China, 2018.
40. Li, J.; Yu, Z.; Wu, J.; Ding, Q.; Xu, W.; Huang, S. The Application of Heat-Shrinkable Fibers and Internal Curing Aggregates in the Field of Crack Resistance of High-Strength Marine Structural Mass Concrete: A Review and Prospects. *Polymers* **2023**, *15*, 3884.
41. G*B/T 50080-2016*; Standard for Test Methods of Performance on Ordinary Fresh Concrete. China Standard Press: Beijing, China, 2017. (In Chinese)
42. *GB/T 50081-2019*; Standard for Test Methods of Concrete Physical and Mechanical Properties. China Standard Press: Beijing, China, 2019. (In Chinese)
43. *SL352-2006*; Test Code for Hydraulic Concrete. China Standard Press: Beijing, China, 2006. (In Chinese)
44. *ACI 544.2R-89*; Measurement of Properties of Fiber Reinforced Concrete. American Concrete Institute: Farmington Hills, MI, USA, 1999.
45. Lyu, S.; Sun, T.; Liu, J.; Ma, Y.; Qiu, C. Toughening effect and mechanism of graphene oxide nanosheets on cement matrix composites. *Acta Mater. Compos. Sin.* **2013**, *31*, 644–651.
46. Xing, W.; Yuan, B.; Wang, X.; Hu, Y. Enhanced mechanical properties, water stability and repeatable shape recovery behavior of Ca2+, crosslinking graphene oxide-based nacre-mimicking hybrid film. *Mater. Des.* **2017**, *115*, 46–51.
47. Dimov, D.; Amit, I.; Gorrie, O.; Barnes, M.D.; Townsend, N.J.; Neves, A.I.S.; Withers, F.; Russo, S.; Craciun, M.F. Ultrahigh Performance Nanoengineered Graphene Concrete Composites for Multifunctional Applications. *Adv. Funct. Mater.* **2018**, *28*, 1705183.
48. Wu, Y.-Y.; Que, L.; Cui, Z.; Lambert, P. Physical Properties of Concrete Containing Graphene Oxide Nanosheets. *Materials* **2019**, *12*, 1707.
49. Labhasetwar, N.K.; Shrivastava, O.P.; Medikov, Y.Y. Mössbauer study on iron-exchanged calcium silicate hydrate: $Ca_{5-x}Fe_xSi_6O_{18}H_2{\cdot}nH_2O$. *J. Solid State Chem.* **1991**, *93*, 82–87.
50. Pellenq, R.J.-M.; Kushima, A.; Shahsavari, R.; Van Vliet, K.J.; Buehler, M.J.; Yip, S.; Ulm, F.-J. A realistic molecular model of cement hydrates. *Proc. Natl. Acad. Sci. USA* **2009**, *106*, 16102–16107.

51. Van Duin, A.C.T.; Dasgupta, S.; Lorant, F.; Goddard, W.A. ReaxFF: A reactive force field for hydrocarbons. *J. Phys. Chem. A* **2001**, *105*, 9396–9409.
52. Hou, D.; Lu, Z.; Zhao, T.; Ding, Q. Reactive molecular simulation on the ordered crystal and disordered glass of the calcium silicate hydrate gel. *Ceram. Int.* **2016**, *42*, 4333–4346.
53. Hou, D.; Zhao, T.; Ma, H.; Li, Z. Reactive molecular simulation on water confined in the nanopores of the calcium silicate hydrate gel: Structure, reactivity, and mechanical properties. *J. Phys. Chem. C* **2015**, *119*, 1346–1358.